

University of Dayton

eCommons

Chemical and Materials Engineering Faculty
Publications

Department of Chemical and Materials
Engineering

8-21-2021

Analytical Model for Electromagnetic Induction in Pulsating Ferrofluid Pipe Flows

Huiyu Wang
University of Oklahoma

John G. Monroe
U.S. Army


Swati Kumari
Sigonas Fruit for Thought

Serhiy O. Leontsev
University of Dayton

Erick S. Vasquez
University of Dayton, evasquez1@udayton.edu

See next page for additional authors

Follow this and additional works at: https://ecommons.udayton.edu/cme_fac_pub

 Part of the [Other Chemical Engineering Commons](#), and the [Other Materials Science and Engineering Commons](#)

eCommons Citation

H. Wang, J.G. Monroe, S. Kumari, S.O. Leontsev, E.S. Vasquez, S.M. Thompson, M.J. Berg, D.K. Walters, K.B. Walters, "Analytical model for electromagnetic induction in pulsating ferrofluid pipe flows," *International Journal of Heat and Mass Transfer*, Volume 175, 2021.

This Article is brought to you for free and open access by the Department of Chemical and Materials Engineering at eCommons. It has been accepted for inclusion in Chemical and Materials Engineering Faculty Publications by an authorized administrator of eCommons. For more information, please contact mschlengen1@udayton.edu, ecommons@udayton.edu.

Author(s)

Huiyu Wang, John G. Monroe, Swati Kumari, Serhiy O. Leontsev, Erick S. Vasquez, Scott M. Thompson, Matthew J. Berg, Dibbon Keith Walters, and Keisha B. Walters

Analytical Model for Electromagnetic Induction in Pulsating Ferrofluid Pipe Flows

H. Wang¹, J. G. Monroe², S. Kumari³, S.O. Leontsev⁴, E.S. Vasquez⁵, S. M. Thompson⁶, M. J. Berg⁷, D. K. Walters¹, K. B. Walters^{8*}

¹ Department of Aerospace and Mechanical Engineering, University of Oklahoma, Norman, Oklahoma 73019, USA

² Engineer Research and Development Center (ERDC), US Army, Vicksburg, Mississippi, 39180, USA

³ Sigonas Fruit for Thought, San Carlos, CA 94070, USA

⁴ University of Dayton Research Institute, University of Dayton, Dayton, Ohio 45469, USA

⁵ Chemical and Materials Engineering Department, University of Dayton, Dayton, Ohio 45469, USA

⁶ Department of Mechanical and Nuclear Engineering, Kansas State University, Manhattan, KS 66506, USA

⁷ Department of Physics, Kansas State University, Manhattan, Kansas 66506, USA

⁸ School of Chemical, Biological and Materials Engineering, University of Oklahoma, Norman, Oklahoma 73019, USA

* corresponding author:
Keisha B. Walters
keisha.walters@ou.edu

Abstract

Energy harvesting processes using ferrofluidic induction—a process that generates voltage via the pulsation of a ferrofluid (iron-based nanofluid) through a solenoid—have received increasing attention over the past decade. In this paper an analytical model is proposed to predict the induced electromotive force (EMF) based on the flow behavior and magnetic properties of a pulsating ferrofluid energy harvesting device. The ferrofluid is treated as an idealized series of discrete magnetic ‘slugs’ within passing through the solenoid, and the model identifies key parameters for describing and optimizing ferrofluidic induction in pulsating pipe flows. The resulting expression for induced EMF as a function of slug position relative to the solenoid is numerically integrated to determine the root mean square (RMS) of EMF during one pulsation cycle. Data from a previously documented study using an experimental induced EMF test rig is analyzed to find corresponding measured values of EMF RMS and used to validate the analytical model. Experimental and analytical results both show an increase in induced EMF with higher pulse frequency, increased number of bias magnets, and reduced spacing between the magnet and solenoid. Furthermore, experimentally measured values of EMF lie within the uncertainty bounds of the model resisted, indicating that induced EMF can potentially be predicted within an order of magnitude for these types of energy harvesting systems.

Keywords: analytical model, ferrofluidic induction, ferrofluid, pulsating flow, energy harvesting, solenoid

Nomenclature

Greek symbols

α – Langevin parameter

ω – angular frequency, Hz
 μ – permeability of the ferrofluid, N/A²
 μ_0 – permeability of the free space, N/A²
 ρ – density, kg/m³
 σ_s – saturation mass magnetization, emu/g, Am²/kg
 χ – susceptibility
 χ_i – initial susceptibility
 λ – dipolar coupling coefficient
 ϕ – volume fraction of the nanoparticles

Symbols

B – magnetic flux density, mT
 d – diameter, m
 D – displacement, m
 E – induced electromotive force (EMF), μV
 f – frequency, Hz
 k – Boltzmann constant
 M_L – Langevin function magnetization, A/m
 M_s – saturation volume magnetization, A/m
 m – magnetic moment of a single nanoparticle, Am²
 m_{slug} – magnetic moment of the slug, Am²
 N – number of solenoid turns
 n – particle concentration (number of iron particles per unit volume), 1/m³
 n_{∞} – mean number of particles in the chain
 R – radius, m
 S – length of the solenoid, m
 T – temperature, K
 t – time, s

Δt – time step, s

V – volume, m³

v – velocity, m/s

v_0 – average velocity, m/s

z – displacement, m

1. Introduction

1.1 Ferrofluids

Ferrofluids have recently attracted attention for use as electromagnetic induction materials and/or thermal transport media in energy harvesting devices [1-10]. Ferrofluids are nanoscale colloidal suspensions of magnetic particles in an organic or aqueous liquid carrier. The surfaces of these particles can be modified with small molecules, surfactants, or polymers to prevent aggregation thus maintaining the stability of the colloidal system despite thermal cycling and even phase change. In comparison to the base carrier liquid, ferrofluids have higher viscosities and thermal conductivities, and consequently demonstrate improved conductive and convective heat-transfer performance [1-2]. Due to their magnetic properties, they also show potential for energy harvesting in thermal management applications. When a ferrofluid moves relative to a solenoid, ferrofluidic induction can occur resulting in electrical voltage generation. Compared to conventional permanent magnets, ferrofluids have the advantage of being suspendable and conforming to any shape channel or vessel; therefore, ferrofluids can potentially be extended to new designs and complex geometries for next-generation electromagnetic energy harvesters.

1.2 Experiments examining ferrofluids for energy harvesting

Most energy harvesting systems employ the sloshing motion of the ferrofluid inside the container. For example, Sansom et al. [1] experimentally investigated the use of commercially available ferrofluids for waste heat removal, power conversion, and energy harvesting applications. In their study, three aqueous ferrofluids were tested in a tubular structure (10 mm ID) placed adjacent to a copper coil inductor with the intention of producing an EMF across the inductor. It was observed that the ferrofluid system acted as a thermal pump and had a thermomechanical conversion efficiency (mechanical movement realized/input thermal energy) of 0.13%. Chen et al. [3] also demonstrated the feasibility of ferrofluid energy harvesting both experimentally and theoretically. In their experiments, a series of cylindrical plastic containers filled with various amounts of ferrofluids were driven through pairs of induction coils. The induced EMF magnitudes increased with the relative fractional ferrofluid-volume inside the container (filling ratio) and the velocity of the ferrofluid moving through the coils. To further investigate the use of ferrofluids for energy harvesting, Bibo et al. [4-5] conducted a series of experiments using an external magnetic field formed by two axially arranged permanent magnets. A time-dependent voltage was generated across a solenoid by the vibratory motion of a container containing magnetized ferrofluid. These results not only demonstrated the potential for ferrofluid-based energy harvesting but also showed the impact of fluid column height, external magnetic field strength, and container acceleration on the measured voltage response; it was concluded that there exists a maximum output voltage for a given column height. Similarly, Kim et al. [6-7] also designed a setup for harvesting energy from the ‘sloshing’ motion of a ferrofluid. The setup consisted of a rectangular container partially filled with ferrofluid, two groups of permanent magnets on the top and bottom of the ferrofluid container, an iron yoke made of ferromagnetic material connected with top and bottom permanent magnets, and two induction coils winding around the yoke. Experiments with this setup showed that the

volume of the ferrofluid inside the container and the permanent magnetic field strength affect the output voltage in the coils.

Our group has previously conducted experiments to investigate electromagnetic induction in a ferrofluid-charged oscillating heat pipe (FF-OHP) [8,9]. This system resulted in a harvested, peak-to-peak solenoid voltage around 1 mV from passive (temperature difference) oscillation in the FF-OHP with the nanoparticle magnetic poles aligned by a bias electromagnetic field. Recently, Choi et al. [10] presented a ferrofluid-based vibration energy harvester with a hybrid triboelectric-electromagnetic operating mechanism. The apparatus included a cylindrical tube half-filled with ferrofluid, two separate aluminum electrodes on the top and bottom of the tube, a 200-turn of wire coil around the outside of the tube, and a permanent magnet at the bottom of the cylinder to provide a bias magnetic field. Compared to conventional solid-solid contact-based generators, the device demonstrated the advantage of operating under very weak vibrations while still generating measurable voltage amplitudes.

1.3 Modeling ferrofluids in magnetic fields

While several different ferrofluid-based electromagnetic energy harvesting apparatuses have been examined experimentally, the ability to compare and optimize designs is limited without predictive analytical and computational modeling methods. To this end there have been only a few prior modeling studies focused on understanding and predicting the behavior of pulsating ferrofluids. In designing an electromagnetic energy harvester for ferrofluid sloshing motion, Kim et al. [7] used finite element numerical simulation to determine the magnetization distribution along/within an energy harvester, with the goal of optimizing magnetization by changing the back yoke shape. Ozbey et al. [11] used commercially available COMSOL Multiphysics[®] software to

simulate ferrofluid flows driven by varying external magnetic fields in small channels. Their modeling results showed that velocity profiles along the tube were not constant and were affected by the magnetic field gradient. Berthier and Ricoul [12] used MATLAB[®] to develop a numerical model for instabilities in ferrofluid plug flow in a capillary tube near a permanent magnet. It was concluded that sudden velocity changes of the ferrofluid slug near the magnet resulted in the ferrofluid slug breaking up into smaller slugs, and this was confirmed by experimental measurements. Papadopoulos et al. [13] performed a numerical analysis of ferrofluid flow in a pipe under the influence of a magnetic field induced by cylindrical coils. In their study, the axial pressure gradient of the ferrofluid flow near the edges of the coils was found to increase linearly with the volumetric concentration of nanoparticles in the ferrofluid.

Besides serving as the working fluid in electromagnetic energy harvesting devices, ferrofluids also have many applications in the biomedical field, and related modeling studies have been performed to study the transport behavior of magnetic particles within an external magnetic field. For example, Furlani et al. [14] presented numerical models to analyze and optimize the magnetofection process, in which magnetic particles are used to deliver gene vectors to target cells for uptake, in multiwell cell culture plate systems. Using these models, several key parameters influencing particle transport and accumulation were identified, such as particle size, magnet-to-wall spacing, position and concentration of particles in a well, and relative orientation of magnetic fields from neighboring magnets. Khashan et al. [15] used computational fluid dynamics (CFD) to design a microfluidic system capable of separating magnetic (or ‘magnetically-labeled’) particles. Integrated flow-invasive soft-magnetic elements were employed for the CFD model. The numerical model helped demonstrate that the magnetofection process has substantial performance

advantages over conventional bioseparation systems by increasing the capture efficiency in specific regions of the channel due to the short-range nature of the magnetic force.

Application of an accurate numerical model can potentially help to drive process improvement, such as the bioseparation method described above. To the authors' knowledge a comprehensive analytical or numerical model has not yet been developed to predict output voltage for use in the analysis and design of ferrofluid energy harvesting processes based on the pulsating motion of a ferrofluid flow. Such a model would allow for the prediction of generated induced electromotive force based on ferrofluid properties, geometric details of the solenoid and pipe/tube system, and any imposed or generated magnetic fields. This analytical study investigates key design parameters that are known to affect ferrofluidic induction, such as the number of bias magnets, magnet spacing, fluid pulse frequency, and ferrofluid particle diameter, to develop a relatively simple analytical model. The resulting model is validated against available experimental data.

2. Analytical Model

2.1 Model Description

To better understand energy harvesting processes using ferrofluid induction due to pulsating flow, an analytical model is developed and validated using the experimental results of Monroe et al. [16]. The basis for this effort is a model developed to describe the electromagnetic induction process from a solid cylindrical magnet with a uniform magnetization M passing through a circular wire ring [17], but extended to apply to a slug of magnetic ferrofluid. The overall approach for the system is similar to one recently demonstrated [18], with ferrofluid slugs acting in place of permanent magnets. Induced EMF is generated by the relative motion between the magnetic slug and the solenoid. As the slug first enters the solenoid, a voltage (induced EMF) is generated due to a sudden change of magnetic flux inside the solenoid. While the slug moves through the solenoid

the induced EMF is zero since the magnetic flux inside the solenoid remains constant. As the slug leaves the solenoid, an induced EMF (opposite sign) is generated due to a sudden inversion of the magnetic flux inside the solenoid (Figure 1).

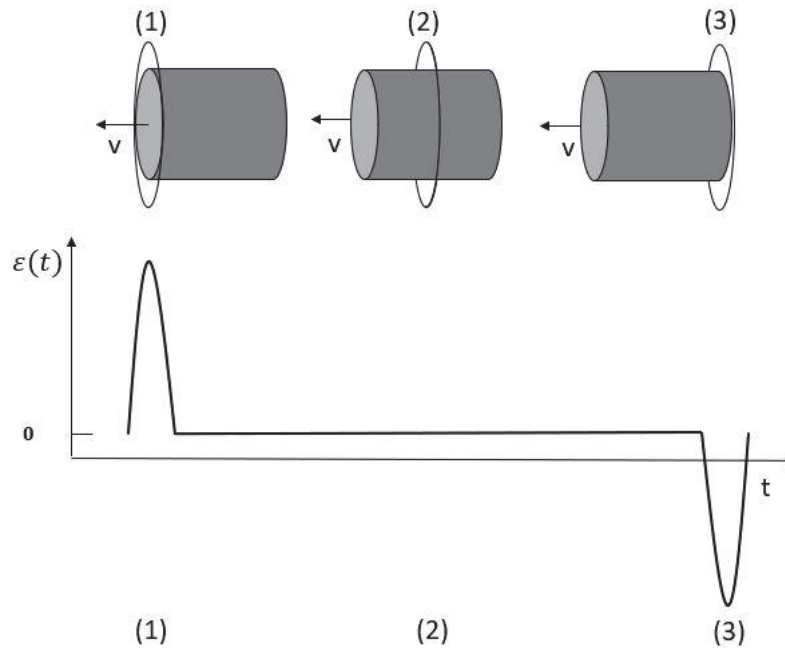


Figure 1. Electromagnetic induction of a cylindrical magnetic slug passing through a circular wire.

As mentioned previously, ferrofluids are composed of two components, magnetic nanoparticles, that are treated as magnetic dipoles, and a liquid carrier. In the absence of an external magnetic field, the magnetic moments of the particles are randomly oriented. When an external magnetic field is applied, the magnetic dipoles align to produce a net magnetic moment that is parallel to the external field, as is shown in Figure 2. The experimental study [16] used to validate the induced EMF analytical model utilized an external magnetic field. Therefore, the analytical model adopts the point of view that the ferrofluid within the tube can be approximated as a cylindrical pseudo-slug consisting of uniformly magnetized material as it flows through the solenoid.

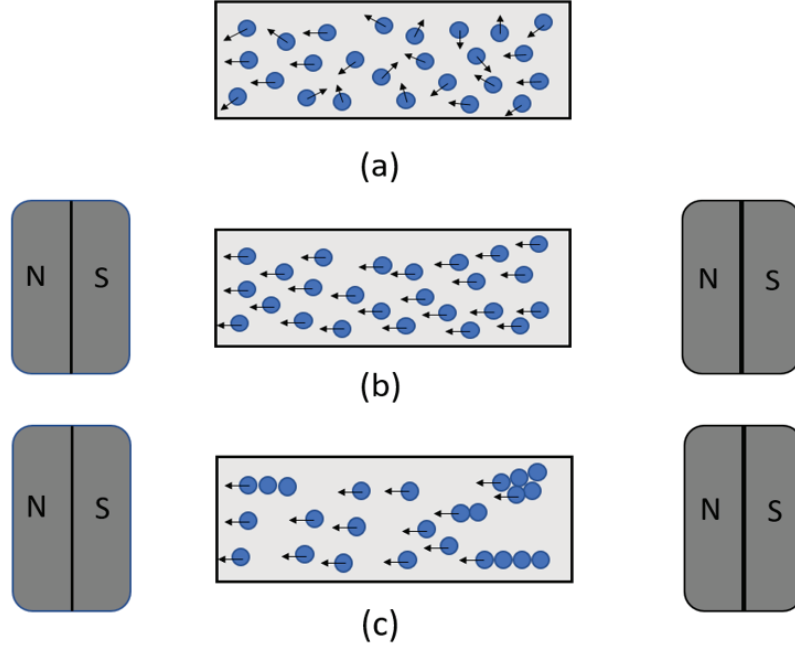


Figure 2. Schematic of the ferrofluids with (a) no bias field, (b) applied bias magnetic field showing alignment of dipole moments of the suspended magnetic nanoparticles, and (c) potential chain structure formation.

The magnetic moment of a cylindrical slug can be calculated as

$$m_{slug} = M_s \times V \quad (1)$$

where m_{slug} is the magnetic moment of the slug, M_s is the volume saturation magnetization of the slug, and V is the volume of the slug.

The analytical model starts with the motion of a point dipole passing through a single loop [19]:

$$e_1(z) = \frac{3\mu p_m R^2 v z}{2(R^2 + z^2)^{5/2}} \quad (2)$$

where μ is the magnetic permeability, p_m is the magnetic moment of the dipole, R is the radius of the solenoid loop, v is the axial velocity of the dipole, and z is the relative axial position between

the dipole and the solenoid loop. Assuming each infinitesimal ‘slice’ of a magnetic slug with length L acts as a dipole, then a differential induced EMF can be defined as

$$de_1(z) = \frac{3\mu m_{slug} R^2 v z}{2L(R^2 + z^2)^{5/2}} dz \quad (3)$$

where the magnetic moment of each differential dipole is assumed to be

$$p_m = \frac{m_{slug}}{L} dz. \quad (4)$$

Defining the slug position z to correspond to the centroid of the slug and integrating over the slug length gives the induced EMF as

$$E_1(z) = \int_{-L/2}^{L/2} \frac{3\mu m_{slug} R^2 v [z+\xi]}{2L[R^2 + (z+\xi)^2]^{5/2}} d\xi. \quad (5)$$

Evaluating the integral yields

$$E_1(z) = \frac{\mu m_{slug} R^2 v}{2L} \left\{ \frac{1}{[R^2 + (z - \frac{L}{2})^2]^{3/2}} - \frac{1}{[R^2 + (z + \frac{L}{2})^2]^{3/2}} \right\}. \quad (6)$$

We now consider the induced EMF of a magnetic slug passing through a solenoid of length S with N loops. Defining the loop spacing as $\Delta = S/(N - 1)$, the induced EMF from all loops can be summed to yield

$$E_{total}(z) = \sum_{i=0}^{N-1} E_1(z + S/2 - i\Delta). \quad (7)$$

Here $z = 0$ corresponds to the center of the solenoid. For cases in which $\Delta \ll R$, the induced EMF through the solenoid can be approximated using an integral over the length of the solenoid,

$$E_{total}(z) = \frac{1}{\Delta} \int_{-N\Delta/2}^{N\Delta/2} E_1(\xi) d\xi, \quad (8)$$

and for $N \gg 1$, the induced EMF can be approximated as

$$E_{total}(z) = \frac{N}{S} \int_{-S/2}^{S/2} E_1(z + \xi) d\xi. \quad (9)$$

Evaluating the integral yields the total induced EMF from a finite length slug passing through a solenoid with N loops, radius R , and length S :

$$E_{total}(z) = \frac{N\mu m_{slug}v}{2LS} \left\{ \frac{z - \frac{L}{2} + \frac{S}{2}}{\left[\left(z - \frac{L}{2} + \frac{S}{2} \right)^2 + R^2 \right]^{\frac{1}{2}}} + \frac{z + \frac{L}{2} - \frac{S}{2}}{\left[\left(z + \frac{L}{2} - \frac{S}{2} \right)^2 + R^2 \right]^{\frac{1}{2}}} - \frac{z + \frac{L}{2} + \frac{S}{2}}{\left[\left(z + \frac{L}{2} + \frac{S}{2} \right)^2 + R^2 \right]^{\frac{1}{2}}} - \frac{z - \frac{L}{2} - \frac{S}{2}}{\left[\left(z - \frac{L}{2} - \frac{S}{2} \right)^2 + R^2 \right]^{\frac{1}{2}}} \right\} \quad (10)$$

For a series of fluid slugs passing through a solenoid, the RMS of induced EMF is then estimated by application of Eq. (10) over the length of a single slug.

2.2 Pulsating motion

In the experimental setup of Monroe et al. [16], the pulsating motion of the ferrofluid through the tube was controlled using a peristaltic pump. This same pump setup was also used to perform a separate flow visualization experiment employing pure water as the working fluid in order to characterize the velocity and flow behavior of a liquid slug. Water was chosen for this visualization experiment since the ferrofluid carrier liquid is water and the pulsating fluid motion could be tracked using the interfaces between the liquid slugs and intentionally introduced air bubbles. To capture the fluid motion, a high-speed camera (Phantom Miro 310, Vision Research Inc., 640x480 resolution, 300 frames per second) was used to collect video and measure the velocity of the fluid at different pumping frequencies. Figure 3 shows a static image of the liquid slug/bubble flow captured using the high-speed camera.

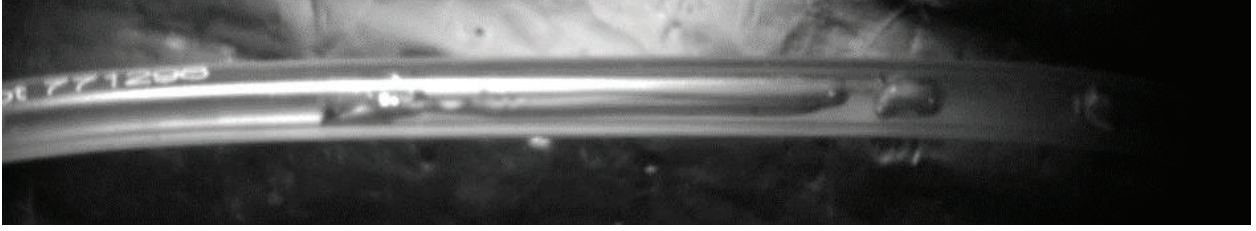


Figure 3. Static image from a high-speed video of water/air slugs pumped at approximately 6 Hz through tubing used in experimental setup [16].

Analyzing the high speed-camera video of the water/air slug flow, the slug displacement, D , for a single pulse averaged 4.11 ± 0.09 cm over the 6-30 Hz frequency range tested. The average velocity of the slug was estimated as $v_0 \cong D/\Delta t$. Since the peristaltic pump consisted of three rollers in sequence, the time period of each flow displacement within the tube was approximately $\Delta t \cong 1/(3f)$, where f is the pumping frequency of the peristaltic pump. Pumping frequencies and associated average pulse velocities for the ferrofluid slug are listed in Table 1. Since fluid pulsation was observed to be nearly harmonic with the cyclic pump frequency, the velocity profile of the magnetic slug moving through the solenoid is assumed to follow

$$v(t) = v_0[1 - \cos(\omega t)] \quad (11)$$

where v_0 is the average velocity and $\omega = 2\pi f$. The displacement of the of the slug is therefore

$$z(t) = v_0 \left[t - \frac{\sin(\omega t)}{\omega} \right] + z_0 \quad (12)$$

where z_0 is the initial position of the slug.

Table 1. Water/air slug pulse velocities for experimentally tested pulsating frequencies.

Pulsating frequency f (Hz)	Time period Δt (s) (+/- stdev)	Average pulsating velocity v_0 (m/s) (+/- stdev)
3	0.11 ± 0.006	0.33 ± 0.02
6	0.05 ± 0.001	0.84 ± 0.02
10	0.03 ± 0.002	1.40 ± 0.07

2.3 Ferrofluid Characterization

To provide appropriate inputs to the analytical model, it is critical to understand the ferrofluid microstructure, i.e., the particle distribution inside the liquid carrier. Some studies [20] have shown that large-sized, chain-like magnetic structures can form within the ferrofluid due to dipolar interactions between the magnetic nanoparticles. Yoon et al. [21] studied the equilibrium structures of ferrofluid aggregates within a magnetic field and showed that dipoles can form chain-like structures which can evolve into larger-scale 2D and 3D multichain assemblies as the system size increases. In this study, transmission electron microscopy (TEM) was employed to characterize the morphological characteristics of the in-house synthesized ferrofluid used in the experiments [16].

A representative TEM image of the magnetic nanoparticles from the ferrofluid is shown in Figure 4. The nanoparticles are dispersed, and the small amount of aggregation observed is likely due to the drying process necessary for TEM imaging. The distribution of measured particle diameters is shown in Figure 5; the average particle diameter was found to be 10.1 nm with a standard deviation of 0.16 nm. With a nanoparticle diameter of 10.1 nm, the volume of each nanoparticle is $5.4 \times 10^2 \text{ nm}^3$. The mass of a single spherical nanoparticle is calculated to be $4.6 \times 10^{-22} \text{ kg}$, using a Fe_3O_4 nanopowder density of 850 kg/m^3 [23]. The experimentally determined physical properties of the in-house synthesized ferrofluid used in this study are summarized in Table 2.

No significant chain-like structures were observed in the ferrofluid TEM images (Fig. 4). This result is expected since with TEM imaging, the sample is not examined under a magnetic field and further is dried prior to being subjected to vacuum conditions. Therefore, with standard TEM it is not possible to visualize the formation of chains or other aggregate structures that might occur for magnetic nanoparticles suspended in solution within a magnetic field.

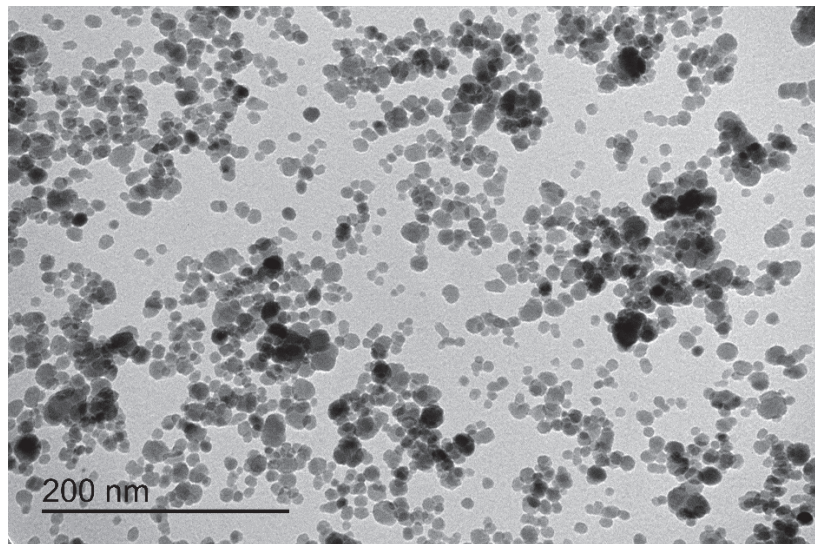


Figure 4. TEM image of Fe₃O₄ magnetic nanoparticles from the in-house aqueous ferrofluid.

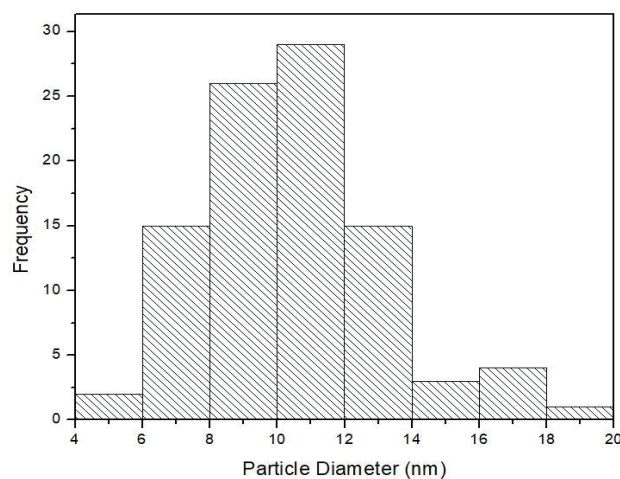


Figure 5. Particle size distribution of iron oxide nanoparticles from the ferrofluid used in the EMF flow loop experiments.

Table 2. Physical properties of in-house synthesized ferrofluid.

Fe ₃ O ₄ weight percentage (%)	10.97
Fe weight percentage (%)	7.94
Density of the ferrofluid (g/cm ³)	1.10
Diameter of nanoparticle (nm)	10.1 ± 0.16

2.4 Magnetic Properties of the Ferrofluid

As mentioned previously, in the absence of an applied magnetic field, nanoparticle magnetic moments are randomly oriented, and the ferrofluid has no net magnetization. Once an external magnetic field is applied, magnetic moments of the dipoles tend to align with the applied field. The net magnetization of the ferrofluid increases as the field strength increases, and at relatively high field strengths, magnetic moments of the dipoles may become completely aligned. A limit occurs when magnetization reaches its saturation value, a phenomenon known as superparamagnetism. The saturation volume-magnetization of a ferrofluid, M_s , depends on magnetic particle concentration (number of Fe₃O₄ particles per unit volume) and the magnetic moment of individual nanoparticles [23]. Considering the magnetic moments of each nanoparticle, the saturation volume-magnetization (M_s) within a volume of ferrofluid can be determined as $M_s = n \times m$ [23]. The magnetic moment of nanoscale Fe₃O₄ powder has been found to range from 12.3 emu/g to 85.8 emu/g [22], therefore the magnetic moment of each nanoparticle, m , is dependent on its mass. The density of nanoscale Fe₃O₄ powder has been found to be 850 kg/m³ [22]. These Fe₃O₄ nanopowder properties were used for calculating the magnetic properties of the in-house ferrofluids used in this study.

Two additional important parameters to consider regarding the magnetization of the ferrofluid are the magnetic susceptibility, χ , and permeability, μ . The initial susceptibility, χ_i , after taking into account the interaction between the magnetic moments of the particles is determined by [23]:

$$\frac{\chi_i(2\chi_i+3)}{\chi_i+1} = 24\phi\lambda \quad (13)$$

and the permeability is

$$\mu = \mu_0(1 + \chi_i). \quad (14)$$

The magnetic properties calculated for the in-house synthesized ferrofluid from the above governing equations are listed in Table 3. As mentioned previously, both experimental and modeling studies have shown that in strong external fields the ferromagnetic nanoparticles tend to form chain-like structures parallel to the field direction [20,21]. Under these conditions the mean number of nanoparticles in the chain can be calculated as

$$n_\infty = [1 - \frac{2}{3} * (\frac{\phi}{\lambda^2}) * e^{2*\lambda}]^{-1} \quad (15)$$

where ϕ is the nanoparticle volume fraction. The dipolar coupling coefficient can be calculated as

$$\lambda = \frac{\mu_0 * m^2}{4 * \pi * d^3 * k * T} \quad (16)$$

where m is the magnetic moment of one single iron oxide particle, μ_0 is the permeability of the free space, $\mu_0 = 4\pi \times 10^{-7} \text{ N/A}^2$, k is the Boltzmann constant, $k = 1.38 \times 10^{-23} \text{ J/K}$, T is the absolute temperature ($T = 293 \text{ K}$), and d is the diameter of magnetic core of the nanoparticle.

Table 3. Magnetic properties of the in-house synthesized ferrofluid containing Fe₃O₄ nanoparticles.

Volume fraction, ϕ (%)	14.5
Particle concentration, n (#/m ³)	$2.65 \cdot 10^{23}$
Magnetic moment of a single nanoparticle, m (emu)	$5.65 \cdot 10^{-18} - 3.94 \cdot 10^{-17}$
Magnetic moment of a single nanoparticle, m (Am ²)	$5.65 \cdot 10^{-21} - 3.94 \cdot 10^{-20}$
Saturation volume-magnetization, M_s (kA/m)	1.5 - 10.4
Saturation mass-magnetization, σ_s (emu/g)	1.35 - 9.43
Dipolar coupling coefficient, λ	$7.66 \cdot 10^{-4} - 3.73 \cdot 10^{-2}$
Initial susceptibility, χ_i (N/A ²)	$8.90 \cdot 10^{-4} - 4.4 \cdot 10^{-2}$
Permeability, μ (N/A ²)	$1.26 \cdot 10^{-6} - 1.31 \cdot 10^{-6}$

The magnetic flux density, B , of the applied bias magnetic field was measured by a DC Gaussmeter (GM-1-ST, AlphaLab, Inc., 0.1 G resolution, 1% accuracy). Since the length of the solenoid was relatively small (about 2 cm), it is assumed that the magnetic flux density inside the solenoid can be approximated as constant. The magnetic flux density in the center of the solenoid is used as the magnetic field strength of the applied bias magnetic field. The locations of the magnets were varied to be either 10.2 cm, 15.2 cm, or 20.3 cm from the center of the solenoid. Resultant magnetic flux densities measured are listed in Table 4. The magnetic flux density of two bias magnets was exactly double that of one bias magnet.

Table 4. Bias magnetic field parameters as a function of magnet number and offset.

Number of Magnets	Magnet Offset / Spacing (cm)	Magnetic Flux Density B (mT)
1	20.3 cm	0.3
2	20.3 cm	0.6
1	15.2 cm	0.7
2	15.2 cm	1.4
1	10.2 cm	2.1
2	10.2 cm	4.2

The magnetization of the ferrofluid in the presence of an applied bias magnetic field and saturation magnetization can be characterized using the Langevin function [23],

$$M_L(B) = n * m * \left[\coth(\alpha) - \frac{1}{\alpha} \right] = n * m * L(\alpha) \quad (17)$$

where n is the particle concentration, m is the magnetic moment of one single iron particle, and $\alpha = (m * B)/(k * T)$ is the Langevin parameter, the ratio of the field interaction to the thermal energy. For each configuration of the magnets shown in Table 4, the magnetization for the ferrofluid “slug” in Eq. (10) was calculated using Eq. (17).

3. Experimental Methods

3.1 Ferrofluid Selection

To investigate the concept of ferrofluid induction, Monroe et al. [16] previously performed a series of experiments that investigated water and two different aqueous Fe_3O_4 ferrofluids as the working fluids, one of the ferrofluids was a commercially-available (Ocean NanoTech) material with a concentration of 10 mg/mL and the second was an in-house synthesized ferrofluid with a concentration of 100 mg/mL. The low-concentration commercial product was found to provide

negligible improvement over pure water (negative control) in terms of EMF generation, so only the in-house ferrofluid experimental data is used as a reference for the present study. The aqueous ferrofluid, containing iron oxide (Fe_3O_4) particles was synthesized as described in [16] with perchloric acid as a surface stabilizer [8].

3.2 Ferrofluid Characterization

The weight percentage of Fe_3O_4 in the synthesized ferrofluid was determined from measuring the ferrofluid mass before and after evaporation of the water and drying of the solids. The iron weight percentage is based on the theoretical stoichiometric value. The density of the ferrofluid was determined by weighing known volumes of the solution. Additional details on the synthesis method and characterization of the aqueous ferrofluid are available in [8].

For transmission electron microscopy (TEM) imaging of the ferrofluid samples, the magnetic nanoparticles were suspended in Nanopure™ water with 20 min of sonication. A drop of the ferrofluid samples (5 μL drop volume) was then placed on 300 mesh carbon film coated TEM grids. After allowing the water to evaporate, the TEM grids were treated with glow discharge before imaging with a JEOL JEM-1400 electron microscope. Image J software was used to measure the outer diameter of the nanoparticles ($n = 60$). The thickness of the surface ligand used to prevent nanoparticle agglomeration was neglected since it was comprised of perchloric acid (HClO_4 , MW = 100.46 g/mol).

3.3 EMF Test Rig Design and Operation

The in-house synthesized ferrofluid, comprised of Fe_3O_4 particles with a particle diameter ~ 10 nm in water, was circulated through 3.2 mm ID Tygon® tubing using a peristaltic pump (Cole Parmer Model 7553-20). The tubing was oriented horizontally to minimize any gravitational

effects. A 1000-turn copper wire solenoid with an outer diameter of 12.7 mm was made from 0.13 mm copper wire wrapped around a tubular core (3.2 mm ID and 127 cm length). To examine the impact of magnet number and position on ferrofluid induction, either one or two neodymium magnets (each a 16.4 cm³ cube) were placed at different distances from the midpoint of the solenoid. The experimental setup parameters, including magnet offset, are listed in Table 5. Figure 6 shows a schematic of the induced electromotive force (EMF) experimental test rig setup.

Table 5. Parameters for ferrofluidic induction experiments performed by Monroe et al. [16].

Parameter	Value(s)
Number of bias magnets	1, 2
Pulse frequency	3 Hz, 6 Hz, 10 Hz
Ferrofluid	Fe ₃ O ₄ + H ₂ O (100 mg/mL)
Magnet offset	10.2 cm, 15.2 cm, 20.3 cm
Solenoid core	Plastic (Tygon [®])
Solenoid number of turns	1000
Solenoid inner diameter	3.2 mm
Solenoid outer diameter	12.7 mm
Solenoid length	20.0 mm

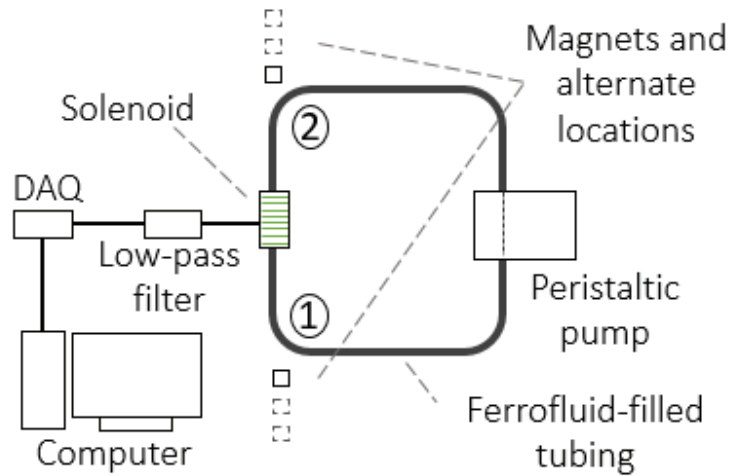


Figure 6. Ferrofluidic induction experimental setup from [16]. Labels ① and ② indicate the magnet positioning/offsets in the induced electromotive force (EMF) flow loop.

4. Results and Discussion

The analytical model presented in section 2 was validated against experimental data of pulsating ferrofluid flow from Monroe et al. [16]. For test rig experiments, the measured induced EMF was generated by a continuous pulsating ferrofluid flow being passed through the solenoid. In the analytical model, the continuous pulsating ferrofluid flow was treated as trains of magnetic “slugs” passing through the solenoid.

For each experimental EMF test rig set-up, the root mean square (RMS) value of the induced EMF measured in [16] was calculated and used as a single metric to quantify effective voltage and validate the analytical model. Examining the RMS value of the induced EMF calculated from the experimental data shown in Table 6, the RMS value of the induced EMF is $13.9 \mu V$ when there is no external magnet or when the pumping frequency is zero. Hence, $13.9 \mu V$ RMS was treated as the baseline noise value for the overall experimental set-up.

Table 6. RMS values of the induced EMF (μV) from experimental data in [16]

Magnetic flux density B (mT)	0 Hz	9 Hz	18 Hz	30 Hz
0	13.9	13.9	13.9	13.9
0.3	13.9	13.8	13.9	14.1
0.6	13.9	14.0	14.1	14.6
0.7	14.0	14.0	14.1	14.9
1.4	13.9	14.1	14.4	16.6
2.1	14.0	14.2	15.3	18.6
4.2	13.9	14.5	17.4	23.8

The RMS value of the noise was subtracted from the measured RMS values allowing the effects of pumping frequency and magnetic flux to be more clearly identified (Table 7). The RMS values of the induced EMF increased with both pumping frequency and magnetic flux density, as expected. Low magnetic flux density (0.3 mT) at either of the lower pumping frequencies (9 Hz and 18 Hz) resulted in nominally zero measured RMS, since the induced EMF due to the pulsating flow was small relative to the baseline noise. At the lowest pumping frequency (9 Hz), the RMS value of the induced EMF was relatively small ($< 1 \mu V$) at all magnetic flux densities. When the pumping frequency was increased to 18 Hz, the RMS value of the induced EMF calculated from the experimental data was $< 1 \mu V$ until the magnetic flux density exceeded 2.1 mT. At all frequencies, the RMS value of the induced EMF increased by a factor of two or more when the magnetic flux density was doubled from 2.1 mT to 4.2 mT. At a pumping frequency of 30 Hz, the induced EMF RMS is $> 1 \mu V$ for all magnetic flux densities was greater than 0.7 mT. Similarly, at a low magnetic flux density (≤ 0.7 mT) the RMS value of the induced EMF was small ($\leq 1 \mu V$) at all pumping frequencies. As the magnetic flux density was increased above 0.7 mT, the RMS value

of the induced EMF increased significantly as a function of increased pumping frequency. The RMS value of the induced EMF experiment increased more than two-fold when the magnetic flux density was doubled.

Table 7. Induced EMF RMS values (μV) adjusted for experimental noise [16]

Magnetic flux density B (mT)	9 Hz	18 Hz	30 Hz
0.3	0	0	0.2
0.6	0.1	0.2	0.7
0.7	0.1	0.2	1.0
1.4	0.2	0.5	2.7
2.1	0.3	1.4	4.7
4.2	0.6	3.5	9.9

Since there are multiple unknown parameters related to the experimental conditions and ferrofluid material properties, a sensitivity analysis was performed to examine the response of the model for induced EMF to small differences in the input variables. Some of the model input variables were well defined in the flow-loop experiment [16]: operating temperature; ferrofluid density; magnetic flux density; tube diameter; solenoid radius; solenoid length; and number of turns of the solenoid. The average slug velocity passing through the solenoid was estimated from video captured by high-speed camera. Values for density and magnetic moment of nanoscale Fe_3O_4 powder in the ferrofluid were obtained from literature sources [22].

Table 8 shows the percentage change in the calculated output voltage for a 1% increase in each of the model input variables. The assumed baseline value for each of the input variables is shown in the table. In terms of general trends, the induced EMF increases with larger Fe_3O_4 particle diameter, magnetic moment of the Fe_3O_4 nanopowder, slug length, and tube diameter. The

calculated EMF decreases as operating temperature, solenoid radius, and solenoid length increase. There is a linear trend between induced EMF and magnetic flux density, ferrofluid density, number of turns in the solenoid, and average slug velocity passing through the solenoid. Compared to other input variables, the particle diameter has the greatest impact with a 3.03% increase in the induced EMF from the analytical model. The slug length has the least impact on the induced EMF with an increase of 0.31% compared with other input parameters.

Table 8. Sensitivity analysis showing the percent change in calculated voltage for a 1% increase in each of the model input parameters

Input parameter	Output Voltage Change
Particle diameter (d) = 10.1 nm	3.03%
Operating temperature (T) = 293 K	-0.99%
Density of ferrofluid (ρ_{ferro}) = 1.10 g/cm ³	1.00%
Magnetic flux density (B) = 1.4 mT	1.00%
Density of nanoscale Fe ₃ O ₄ powder = 850 kg/m ³	1.00%
Magnetic moment of Fe ₃ O ₄ powder = 49.05 emu/g	2.01%
Diameter of the tube (D) = 3.2 mm	2.01%
Radius of the solenoid (R) = 3.975 mm	-0.36%
Length of the slug (L) = 2 cm	0.31%
Length of the solenoid (S) = 2 cm	-0.97%
Number of turns of the solenoid (N) = 1000	1.00%
Average slug velocity (v_0) = 0.84 m/s	1.00%

In the analytical model, an important consideration is determination of the effective length and volume of the magnetic ferrofluid slug. The diameter of the slug is assumed to be equal the tube internal diameter, $d = 3.2$ mm. Hence the volume of the ferrofluid slug can be calculated as $V =$

$\frac{\pi d^2 L}{4} = [8.04 \times 10^{-6} m^2] \times L$. The choice of slug length is not straightforward. Here we consider

two characteristic length scales in the current setup, the length of the solenoid, $L = S = 2 \text{ cm}$, and the distance traveled by the fluid during one pulsation cycle, $L = 4.1 \text{ cm}$. For both lengths, the estimate of RMS of induced EMF was computed by numerically integrating Eq. (10) along the entire length of the slug. A minimum and maximum result was found by considering the valid ranges for key ferrofluid material properties, namely the values of magnetic moment for a single nanoparticle, m , and permeability, μ , listed in Table 3. Using the low and high parameter values resulted in the EMF bounding values as determined by the analytical model. The slug velocity was assumed to be equal to the mean fluid velocity, v_0 .

Figures 7-12 show the model prediction of induced EMF for the three pumping frequencies at each of the magnetic flux densities tested. The difference between the minimum and maximum model prediction due to uncertainty in the ferrofluid properties is approximately two orders of magnitude for all cases. Relative to the range of results from considering material property differences, the impact on the model results from the two different slug lengths is small. Notably, the experimental data falls between the model bounds for all cases except for the two lowest frequencies when $B = 3 \text{ mT}$. For this case, as discussed above, the induced EMF was too small in the experiments to be differentiated from the background noise (Table 7), so these data points are not included in the plots.

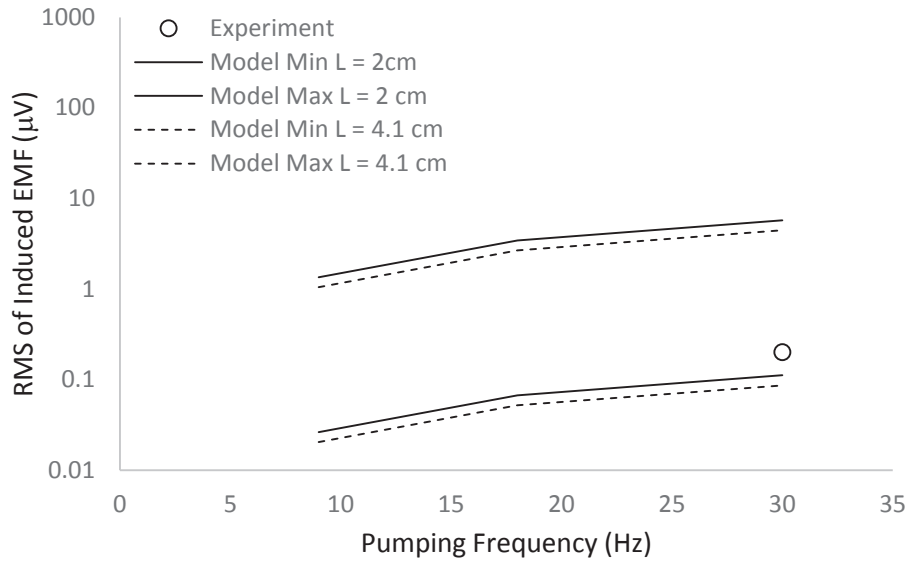


Figure 7. Comparison of the experimental and analytical values of induced EMF as a function of pumping frequency for magnetic flux density $B = 0.3 \text{ mT}$.

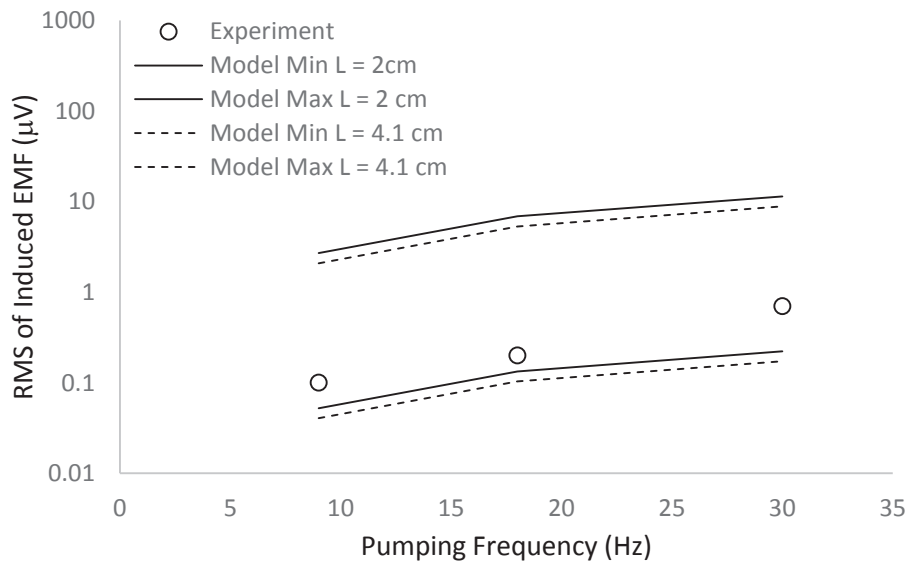


Figure 8. Comparison of the experimental and analytical values of induced EMF as a function of pumping frequency for magnetic flux density $B = 0.6 \text{ mT}$.

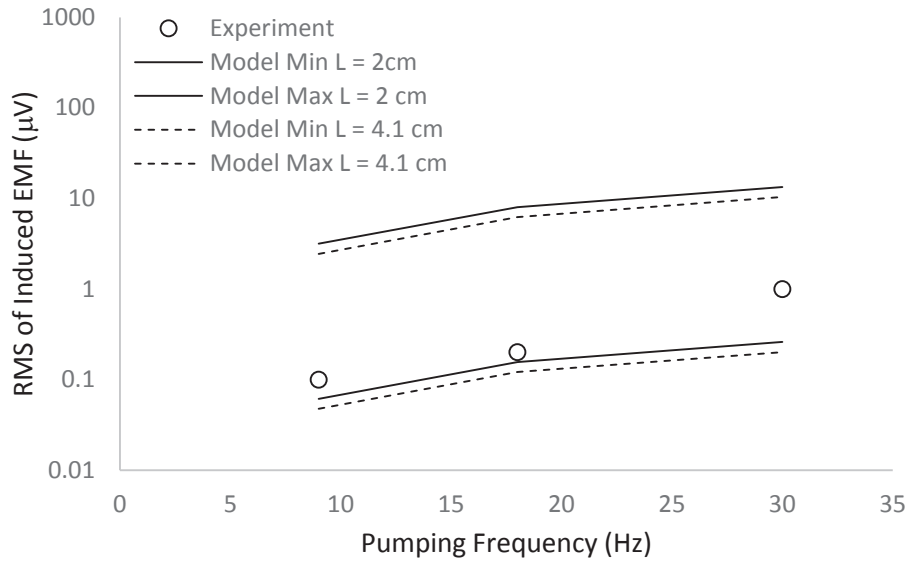


Figure 9. Comparison of the experimental and analytical values of induced EMF as a function of pumping frequency for magnetic flux density $B = 0.7 \text{ mT}$.

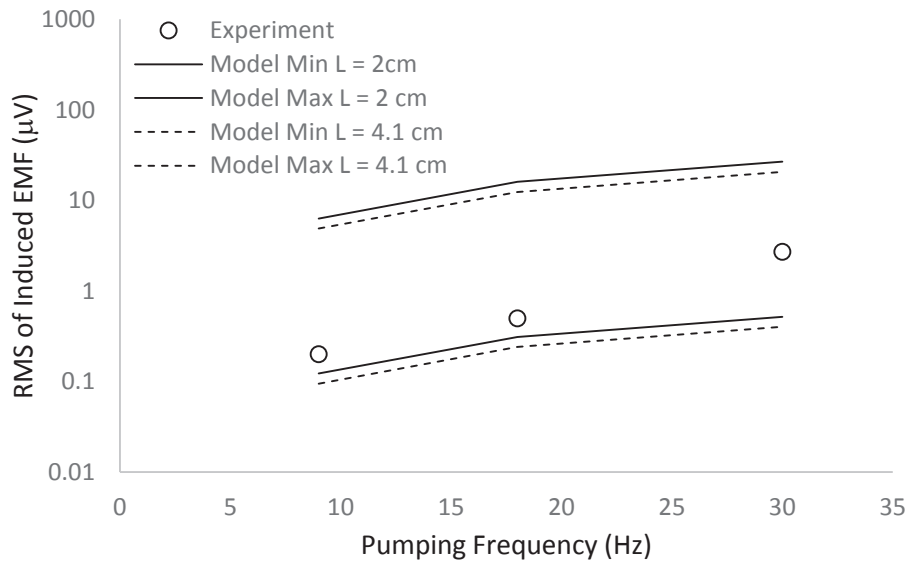


Figure 10. Comparison of the experimental and analytical values of induced EMF as a function of pumping frequency for magnetic flux density $B = 1.4 \text{ mT}$.

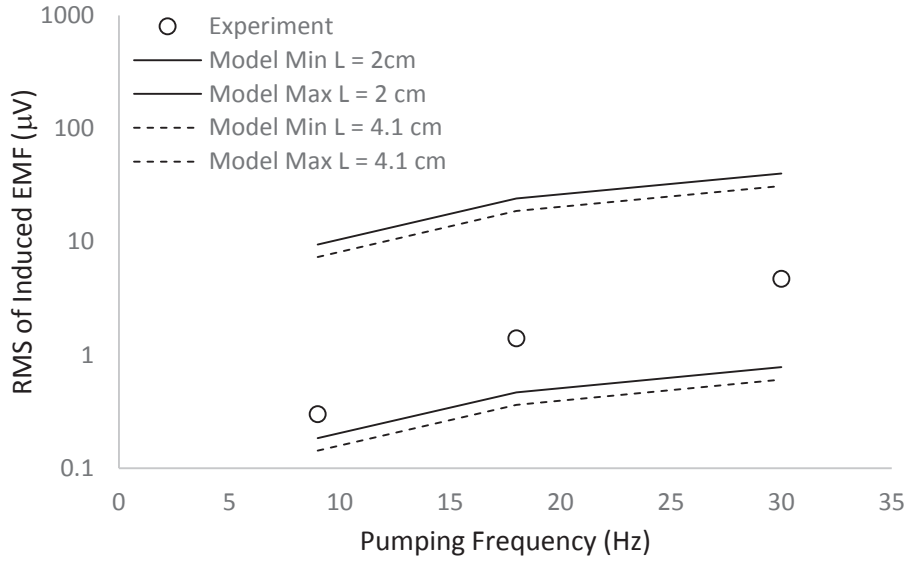


Figure 11. Comparison of the experimental and analytical values of induced EMF as a function of pumping frequency for magnetic flux density $B = 2.1 \text{ mT}$.

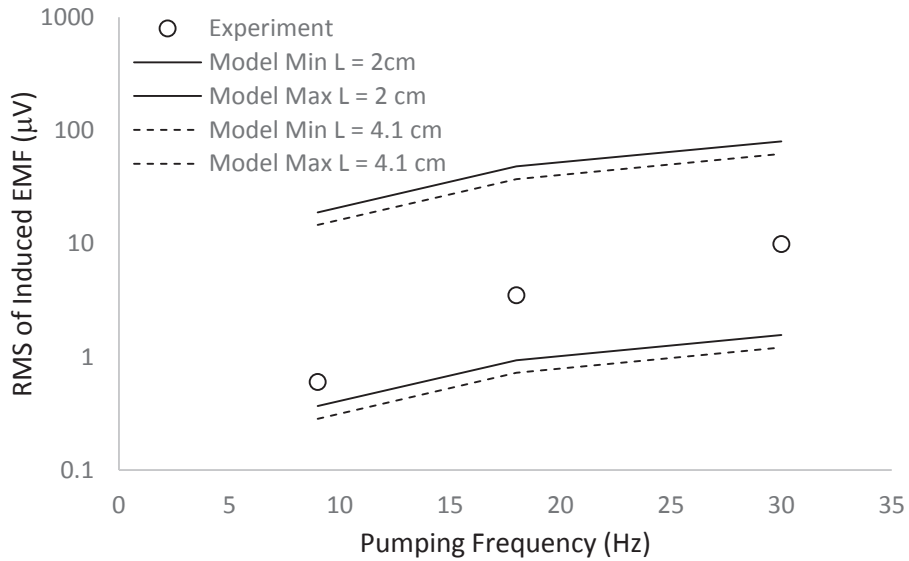


Figure 12. Comparison of the experimental and analytical values of induced EMF as a function of pumping frequency for magnetic flux density $B = 4.2 \text{ mT}$.

In addition to the uncertainty in the ferrofluid properties discussed above, additional error in the model is likely present due to difficulties in accurately quantifying the slug velocity when

the magnetic field is applied. There is likely inaccuracy due to the imaging method used to obtain the water/air slug velocity. In addition, differences in velocity are expected between the ferrofluid flow and water/air mixed flow inside the tube. In the high-speed camera experiment, the water/air flow was driven only by the pump without any external force. In the ferrofluid flow-loop experiment, there is an additional attractive force on the flow due to the bias magnetic field and also more complex multiphase flow. The additional force will tend to accelerate the fluid motion along the direction of the bias magnetic field, especially when the ferrofluid first enters the bias magnetic field (position ① or ② in Figure 6). This acceleration is due to a large pressure drop along tube axis which occurs when there is a large magnetic field gradient. This phenomenon was confirmed by Papadopoulos et al. [13] in their numerical model of the ferrofluid pipe flow under an external magnetic field generated by a coaxial finite solenoid. In their model, this large pressure drop was present at the entrance and exit of the solenoid coils, where large field-gradients exist. In the system investigated herein, this pressure drop occurs close to the surface of the bias magnet where there is a large magnetic gradient. As a result, the actual velocity of the ferrofluid ‘slug’ passing through the solenoid should be greater than that measured for water/air flow in the high-speed video. Examining Eqn. (10), an increase in the speed of the ‘slug’ passing through the solenoid will result in an increase the RMS value of the induced EMF.

Both the experimental data and analytical model show the same trend with the RMS value of the induced EMF increasing as a function of pulsating frequency, since higher pulse frequencies lead to faster relative motion between the solenoid and magnetic slug. Also, the induced EMF is demonstrated both analytically and experimentally to increase with a stronger external magnetic field as a higher percentage of the ferrofluid nanoparticle moments are aligned. Besides, the analytical model shows that the induced EMF would decrease with operating temperature. These

outcomes relating higher pulsating frequencies and external magnetic fields to larger induced EMF agree well with the experimental results from other researchers [3-5]. By adjusting these parameters, the magnetic moment of slug and subsequently the induced EMF across the solenoid can potentially be controlled and/or optimized.

Conclusions

The analytical model developed in the present work predicts induced EMF due to a pulsating ferrofluid passing through solenoid-equipped tubing. The basis of the model is the assumption that the pulsating fluid is analogous to a series of cylindrical slugs moving through the induction coil. Starting from the expression for induced EMF from a single point dipole, an expression for EMF versus relative position between the slug centroid and solenoid centroid is obtained. The expression can then be integrated to determine the RMS value of EMF for a given set of conditions.

The model inputs include properties of the ferrofluid, magnetic field, solenoid, and fluid flow. As a consequence, it potentially can be tailored to a wide range of EMF generation systems. Experimental data from an energy harvesting process that employed pulsating ferrofluid motion driven by a peristaltic pump was used to validate the model. Uncertainty in the model inputs was included by obtaining minimum and maximum prediction of induced EMF for each test case. The two extrema were found in the present case to differ by approximately two orders of magnitude.

The analytical model generated was able successfully predict induced EMF from a solenoid for pulsating ferrofluids. The trends with respect to both magnetic flux density and pumping frequency were correctly reproduced, and the experimental EMF values were between the minimum and maximum for all cases, with the exception of the two operating conditions for which

the experimental values were nominally zero. Overall, the results suggest that the modeling approach adopted here is valid for these magnetic fluid-induced energy harvesting configurations, although further work is needed to fully validate and optimize the modeling methodology for general ferrofluid energy scavenging applications.

Acknowledgments

This work was funded in part by the National Science Foundation (CBET-1403872, CBET-0923474, IIA-1430364, EPS-0903787 and DBI-1126743). The authors would also like to thank Dr. Santanu Kundu (Mississippi State University) for use of the high-speed video equipment and Ying Xiao (Louisiana State University) for collecting the TEM images. The US Army Engineer Research and Development Center (ERDC) did not fund or endorse the research disclosed herein; any opinions, findings, conclusions, or recommendations expressed herein do not necessarily reflect the views of ERDC.

References

- [1] C.L. Sansom, P. Jones, R.A. Dorey, C. Beck, A. Stanhope-Bosumpim, J. Peterson, "Synthesis and characterization of $Mn_{0.5}Zn_{0.5}Fe_2O_4$ and Fe_3O_4 nanoparticle ferrofluids for thermo-electric conversion," *Journal of Magnetism and Magnetic Materials* (2013) 335:159-162.
- [2] M. Yarahmadi, H. Moazami Goudarzi, M.B. Shafii, "Experimental investigation into laminar forced convective heat transfer of ferrofluids under constant and oscillating magnetic field with different magnetic field arrangements and oscillation modes," *Experimental Thermal and Fluid Science* (2015) 68:601-611.

- [3] Ching-Yao Chen, Sheng-Yan Wang, Chi-Ming Wu, Chung-Hao Lin, Kuo-An Huang, "Characteristics of electromagnetic induction by moving ferrofluids," *Magnetohydrodynamics* (2012) 48(3):567-580.
- [4] A. Bibo, R. Masana, A. King, G. Li, M.F. Daqaq, "Electromagnetic ferrofluid-based energy harvester," *Physics Letters A* (2012) 376:2163-2166.
- [5] S.F. Alazemi, A. Bibo, M.F. Daqaq, "A ferrofluid based energy harvester: An experimental investigation involving internally-resonant sloshing modes," *Eur. Phys. J. Special Topics* (2015) 224:2993-3004.
- [6] Dae Woong Oh, Dong Yoon Sohn, Doo Gyoon Byun, Young Sun Kim, "Analysis of Electromagnetic Force Characteristics and Device Implementation for Ferrofluid Based Energy Harvesting System," 2014 17th International Conference on Electrical Machines and Systems (ICEMS), Oct. 22-25, 2014, Hangzhou China
- [7] Young Sun Kim, "Analysis of Electromotive Force Characteristics for Electromagnetic Energy Harvester using Ferrofluid," *Journal of Magnetism* (2015) 20(3):252-257.
- [8] J.G. Monroe, E.S. Vasquez, Z.S. Aspin, K.B. Walters, M.J. Berg, S.M. Thompson, "Electromagnetic induction by ferrofluid in an oscillating heat pipe," *Applied Physics Letters* (2015) 106:26931.
- [9] J. Gabriel Monroe, Swati Kumari, John D Fairley, Keisha B Walters, Matthew J Berg, Scott M Thompson, "On the Energy Harvesting and Heat Transfer Ability of a Ferro-Nanofluid Oscillating Heat Pipe," *International Journal of Heat and Mass Transfer* (2019) 132:162-171, DOI: 10.1016/j.ijheatmasstransfer.2018.11.096.

- [10] Myeong-Lok Seol, Seung-Bae Jeon, Jin-Woo Han, Yang-Kyu Choi, "Ferrofluid-based triboelectric-electromagnetic hybrid generator for sensitive and sustainable vibration energy harvesting," *Nano Energy* (2017) 31:233–238.
- [11] A. Ozbey, M. Karimzadehkhoei, S. E. Yalcin, D. Gozuacik, A. Kosar, "Modeling of ferrofluid magnetic actuation with dynamic magnetic field in small channels," *Microfluid Nanofluid* (2015) 18:447–460.
- [12] Berthier J, Ricoul F, "Numerical modeling of ferrofluid flow instabilities in a capillary tube at the vicinity of a magnet," *Proceedings of 2002 Modeling and Simulation of Microsystem Conference* (2002), pp 22–25.
- [13] P.K. Papadopoulos, P. Vafeas, P. M. Hatzikonstantinou, "Ferrofluid pipe flow under the influence of the magnetic field of a cylindrical coil," *Physics of Fluids* (2012) 24:122002.
- [14] E. P. Furlani, X. Xue, "Field, force and transport analysis for magnetic particle-based gene delivery," *Microfluid Nanofluid* (2012) 13:589–602; DOI 10.1007/s10404-012-0975-x.88
- [15] S. A. Khashan, A. Alazzam, E.P. Furlani, "Computational Analysis of Enhanced Magnetic Bioseparation in Microfluidic Systems with Flow-Invasive Magnetic Elements," *Scientific Reports*, 4:5299, DOI: 10.1038/srep05299.
- [16] G. Monroe, E. Vasquez, Z. Aspin, J. Fairly, K. Walters, "Energy Harvesting via Ferrofluidic Induction," *Proceeding of SPIE 9493, Energy Harvesting and Storage: Materials, Devices, and Applications VI*, 94930G (18 May 2015); DOI: 10.1117/12.2178419.
- [17] D. J. Griffiths, *Introduction to Electrodynamics*, pp 314-315.

- [18] H. Moazami Goudarzi, M. Yarahmadi, M. Shafii, "Design and construction of a two-phase fluid piston engine based on the structure of fluidyne," *Energy* (2017) 127:660–670.
- [19] S. Taylor, V. Leus, "The magneto-kinematic effect for the case of rectilinear motion," *European Journal of Physics* (2012) 33:837–852.
- [20] K. Butter, P.H.H. Bomans, P.M. Frederik, G.J. Vroege, P. Philipse, "Direct observations of dipolar chains in iron ferrofluids by cryogenic electron microscopy," *Nature Materials* (2003) 2:88-91.
- [21] Mina Yoon, David Tomanck, "Equilibrium structure of ferrofluid aggregates," *J. Phys.: Condes. Matter* (2010) 22:4551054-4551060.
- [22] Jun Wang, Jingjun Sun, Qian Sun, Qianwang Chen, "One-step hydrothermal process to prepare highly crystalline Fe_3O_4 nanoparticles with improved magnetic properties," *Materials Research Bulletin* (2003) 38:1113-1118.
- [23] R. E. Rosensweig, Ferrohydrodynamics, Cambridge University Press (1985).

Declaration of interests

The authors declare that they have no known competing financial interests or personal relationships that could have appeared to influence the work reported in this paper.

The authors declare the following financial interests/personal relationships which may be considered as potential competing interests:

CRedit authorship contribution statement

H. Wang: Model Development, Data Generation, Writing – original draft; Writing - review and editing. **J. G. Monroe:** Writing - review and editing. **S. Kumari:** Magnetic nanoparticle synthesis and characterization. **S.O. Leontsev:** Magnetometer experiments on ferrofluid samples. **E.S. Vasquez:** Magnetic nanoparticle synthesis, Ferrofluid characterization; Writing - review & editing. **S. M. Thompson:** Writing - review and editing, Funding acquisition. **M. J. Berg:** Model Development; Writing - review and editing. **D. K. Walters:** Supervision, Writing - review & editing, Funding acquisition. **K. B. Walters:** Model Development, Conceptualization, Supervision, Writing – original draft, review, and editing, Funding acquisition.